# Observations of Effects of Global Dust Storms on Water Vapor in the Southern Polar Region of Mars.

Alexey A. Pankine[a,*], Cecilia Leung[b], Leslie Tamppari[b], Martinez, German[c], Giuranna, Marco[d], Piqueux, Sylvain[b], Smith, Michael[e], Trokhimovskiy, Alexander[f].

[a]Space Science Institute, Boulder, Colorado, USA

[b] NASA Jet Propulsion Laboratory, California Institute of Technology, Pasadena, CA, USA

[c]Lunar and Planetary Institute, Houston, Texas, USA

[d]Istituto di Astrofisica e PlanetologiaSpaziali (IAPS) – Istituto Nazionale di Astrofisica (INAF), Rome, Italy

[e]NASA Goddard Space Flight Center, Greenbelt, MD, USA

[f]Space Research Institute RAS, Moscow, Russia

*Corresponding Author E-mail address: apankine@spacescience.org

Pages: 46

Tables: 0

Figures: 11

**Proposed running head:** .

**Editorial correspondence to:**

Dr. Alexey Pankine

E-mail address: apankine@spacescience.org

## ABSTRACT

Martian Global Dust Storms (GDS) can significantly affect the water cycle in the lower atmosphere (0–40 km). We compare evolution of water vapor abundances, dust opacity and surface temperatures in the Southern Polar Region (SPR) during GDS years of MY25, MY28 and MY34 relative to years without GDS. During all GDS years, the vapor abundances decrease in the lower atmosphere in the SPR following the storm. Our results suggest that this decrease could be the result of vapor moving to higher altitudes and not being available for poleward transport in the lower atmosphere.


## PLAIN LANGUAGE SUMMARY

This work provides the first look at how water vapor in the Martian polar atmosphere reacts to large dust storms in different years. Measurements of water vapor, atmospheric dust and surface temperatures collected by different spacecraft instruments in years with and without large dust storms are compared. These comparisons inform our understanding of how Martian water vapor is transported through the atmosphere and how it interacts with the surface.

## KEY POINTS

Water vapor abundances over the Southern Polar Region of Mars are reduced following a Global Dust Storm.

The decrease in water vapor abundances could be caused by disruption of southward vapor transport by a Global Dust Storm.


**Key Words:** Mars, atmosphere; Mars, climate; Abundances, atmospheres.

## 1. Introduction

The present-day water cycle is a window into the history of water on Mars. A key scientific question is understanding how Mars transitioned from an early history where water was in greater abundance, to today's arid environment (Banfield et al., 2020).

All of the known water on present-day Mars is tied up in the north and south polar ice caps, in the subsurface, and in the atmosphere. Water vapor, in particular, is the most variable trace gas observed on Mars, being affected by atmospheric circulation, cloud formation, as well as by interactions with the regolith and surface ice deposits on seasonal and diurnal cycles. The global water cycle on Mars is driven largely by the annual exchange between the north polar ice cap and the atmosphere (e.g., Haberle et al., 2017). The presence of a perennial $CO_2$ ice layer near the south pole has led to the hypothesis of a permanent cold trap for water vapor, where up to ~$10^{10}$–$10^{11}$ kg of water, representing 1–10% of the seasonal inventory of water vapor, may be deposited at the south pole each year (Jakosky, 1983; Brown et al., 2014). Placing limits on the modern-day water deposition rate in the Southern Polar Region (SPR) will provide important insight into the mass balance of volatiles and the stability of the polar ice cap, a key to unraveling the climatic history of Mars.

Along with water, dust is another important climatic parameter in the Martian atmosphere. Coupling between the water and dust cycles is particularly evident during global dust storms (GDSs), as the radiative effects of dust can dramatically alter atmospheric and surface temperatures, leading to significant modifications in the global circulation, vertical water distribution, water-ice cloud saturation conditions, as well as surface-atmospheric exchange rates (Guzevich et al., 2019; Savijarvi et al., 2020). A number of recent studies have highlighted the role of GDSs in enhancing the rate of water escape, by injecting water from the lower atmosphere (0–40 km) into the middle atmosphere (40–150 km). Vandaele et al. (2019) and Fedorova et al. (2020) observed an increase in southern hemisphere $H_2O$ at altitudes between 40–80 km during a planet-encircling dust storm. This phenomenon is thought to result from warmer atmospheric temperatures causing stronger atmospheric circulation and prohibiting water ice cloud formation. Chaffin et al. (2014; 2017) and Heavens et al. (2018) further linked the increase in atmospheric water content at high altitudes to an increase in hydrogen escape from Mars' atmosphere. Montmessin et al. (2017) found that the mass transfer between the well-mixed lower atmosphere and upper atmosphere (above ~150 km) where hydrogen can freely escape appears to occur on seasonal timescales, much shorter than theoretical predictions. These studies emphasize the strong coupling between (1) the water and dust cycles, and (2) the interconnections between the lower atmosphere and the upper atmosphere. The study presented here investigates these interdependences by doing a systematic and detailed assessment of the vapor and dust behavior during GDS years.

We propose that just as global dust storms have been shown to significantly affect the water cycle in the middle atmosphere, they could similarly influence the water cycle in the lower atmosphere. While an increase in middle atmospheric water was observed during global dust storms, several studies noted a decrease in the overall water column abundance in the southern polar region (SPR) during a GDS. The three most recent (at the time of writing in the spring of 2023) major global dust storms on Mars occurred during Mars Years (MY) 25 (2001), 28 (2007), and 34 (2018). Pankine and Tamppari (2019) showed that in MY25 column vapor abundances between 50°S–90°S were lower by ~5–10 pr-μm than in MY24 and MY26 (adjacent years without GDS) after $L_s$~250° during the decay phase of the GDS. These interannual difference are in response specifically to the effects of the MY25 GDS. Similarly, Smith et al. (2018) and

Trokhimovskiy et al. (2015) reported a decrease in CRISM and SPICAM water vapor abundances in the SPR, respectively, during the MY28 GDS relative to non-GDS years.

Pankine and Tamppari (2019) put forth two possible mechanisms for the reduction in observed column water vapor abundances in the south polar region during a GDS: (1) Changes in surface temperatures (lower daytime surface temperatures and higher nighttime surface temperatures) during the GDS at latitudes between 50°S–60°S could lead to an overall reduction in regolith vapor desorption rates; (2) Changes in atmospheric circulation could reduce southward transport of water vapor from the southern mid-latitudes into the SPR during southern spring. The first hypothesis reduces the atmospheric vapor column in the SPR by sequestering water in the subsurface, while the second reduces the vapor column by preventing atmospheric water from entering the SPR.

In this paper, we quantify the water vapor deficit in the SPR observed during the three most recent major GDSs on Mars occurred during MY25, MY28, and MY34, and compare the variabilities across the three global dust storm years. For the purpose of this study, our definition of the Southern Polar Region expands beyond traditional latitudinal boundaries to include unfrosted surfaces spanning from 40°S to the polar cap edge. The SPR defined in this way includes Hellas and Argyre Planitias, which may have significant effect on the circulation and vapor concentrations in the area (Steele et al., 2014). We examine and compare the water vapor abundances, dust optical depths, and surface temperatures ($T_{surf}$), from latitudes 40°S–90°S between $L_s$ =180°–360° during the three most recent GDS years, plus adjacent non-GDS years. The paper is organized as follows: Section 2 provides an overview of the datasets used in this study, Section 3 presents the results, which are discussed in Section 4, and conclusions are presented in Section 5.

## 2. Instruments and Datasets

To assess the variabilities and characterize differences and similarities in water vapor abundances, atmospheric dust opacities, and surface temperatures, we use datasets from the Mars Global Surveyor (MGS) Thermal Emission Spectrometer (TES), the Mars Express (MEX) Spectroscopy for the Investigation of the Characteristics of the Atmosphere of Mars (SPICAM), Mars Odyssey (MO) Thermal Emission Imaging System (THEMIS), the Mars Reconnaissance Orbiter (MRO) Compact Reconnaissance Imaging Spectrometer for Mars (CRISM) and Mars Climate Sounder (MCS) instruments, as well as the Nadir and Occultation for MArs Discovery (NOMAD) instrument onboard the ExoMars Trace Gas Orbiter (TGO) spacecraft. We have considered observations collected by Planetary Fourier Spectrometer Long Wavelength channel (PFS/LW) aboard the Mars Express (MEx) spacecraft (Giuranna et al., 2021; Pankine, 2022b), but unfortunately the coverage of the SPR in MY28 and MY34 was not sufficient for analysis. Figure 1 shows a summary of GDS occurrences and the availability of the data products used in this study as a function of Mars year. These datasets are discussed below. To compare behavior of vapor abundances, dust opacities and surface temperatures in different years, we average the observations from each dataset into 10°-wide zonal bands from 40°S to 90°S, and 5° $L_s$ time-interval bins. Hundreds of observations are typically averaged per spatio-temporal bin resulting in statistically robust estimates of average quantities. Vapor abundances and dust opacities were scaled by surface pressure to remove effects of topography and possible biases associated with differences in longitudinal coverage. Only data retrieved above surfaces with $T_{surf}$> 155 K were included in the analysis. Using this surface temperature criterion enables a simple approximation for selection of locations that are not covered by seasonal $CO_2$ frost. Comparison of locations of seasonal cap boundaries derived with this simple criterion to locations of boundaries calculated by Piqueux et al. (2015) from analysis of diurnal variability of surface temperature shows close correspondence.

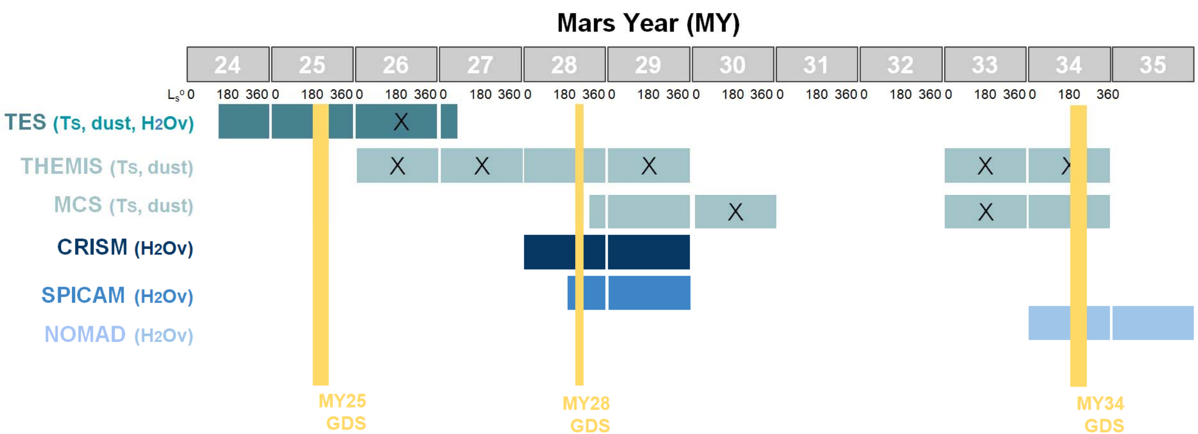


**Figure 1. Occurrences of GDSs and usage of datasets between MY24 to MY34.**

### *2.1 MGS TES*

TES was an infrared spectrometer aboard the MGS spacecraft operating in the spectral range of 200–1700 $cm^{-1}$ (6–50 μm, Christensen et al., 2001). TES made observations of Mars from a near-polar sun-synchronous orbit and operated in both limb-scanning and nadir-pointing viewing geometries. Spectra of the Martian surface and atmosphere were collected at two local times: ~2 am and ~2 pm. The complete TES dataset, consisting of ~200 million thermal infrared spectra, covers the time period from MY24 at $L_s$=104° to MY27 at $L_s$=82° (Smith, 2004; 2008). In this study, we use TES surface temperatures, atmospheric dust opacities (Smith, 2004; Pankine et al., 2023), and water vapor column abundances (Pankine and Tamppari, 2019) retrieved from nadir observations over the SPR in MY24 and MY25.

### *2.2 MEX SPICAM IR*

The SPICAM IR spectrometer on the MEX spacecraft started observing Mars at the end of MY26 (January 2004). SPICAM IR is dedicated primarily to nadir measurements of water vapor abundance (Korablev et al., 2006). It is one of two channels of the SPICAM UV-IR instrument. SPICAM IR analyzes solar radiation reflected from the surface of Mars and modified by atmospheric absorptions in the 1.0–1.7 μm spectral range. Local times of SPICAM IR observations vary through its mission due to the eccentricity of the MEX spacecraft's orbit. In this work we utilize water vapor abundances for MY28 and MY29. In both MY28 and MY29 SPICAM IR observations in the SPR cover all local hours throughout the second half of the year ($L_s$=180°–360°). We use SPICAM IR observations for local hours between 6 am and 6 pm.

### *2.3 MO THEMIS*

THEMIS aboard the MO spacecraft observes Mars at nine wavelengths centered from 671 $cm^{-1}$ to 1470 $cm^{-1}$ (6.8 to 14.9 μm), and in visible/near-infrared bands centered from 0.42 to 0.86 μm (Christensen et al., 2004). THEMIS observations began in MY25 at $L_s$ = 330° (February 2002). Observations made by THEMIS in the nine infrared spectral bands enable the retrieval of the atmospheric dust opacity and surface temperature. The local times of the THEMIS observations varied between roughly 3 pm and 6 pm for MY26–MY29 (Smith, 2009), prior to an orbit node change. In this work we use THEMIS dust opacities and surface temperatures collected in MY28 at ~4–6 pm for comparison with MCS data in MY29.

### *2.4 MRO CRISM*

CRISM is a visible/near-IR imaging spectrometer on the MRO spacecraft, which began taking data in MY28 at $L_s$~101° (September 2006) and ended on $L_s$~222° in MY36 (May 7, 2022) (Murchie et al., 2007; Seelos et al., 2023). CRISM operated in the spectral range of 0.36–3.92 μm. Spectra were taken in nadir and off-nadir geometry. Near-infrared reflectance spectra taken by CRISM can be used to retrieve atmospheric column abundances of $CO_2$, CO and water vapor. Local times of CRISM observations are ~3 pm. In this work we use CRISM water vapor abundances in MY29 as the reference observation for a non-GDS year.

### *2.5 MRO MCS*

MCS is a radiometer on the MRO spacecraft that observes Mars in nine spectral intervals with 20 $cm^{-1}$ and broader spectral passbands in the range 0.3–45 μm (McCleese et al., 2007). Each spectral band is represented by a 21-element linear array. MCS can observe in limb, nadir and on planet (8−10° below limb) viewing geometry modes. Limb observations provide vertical profiles of temperature and aerosols for altitudes from ~10 to 80 km, while nadir views provide column abundances of aerosols and surface temperatures. Local times of MCS observations are approximately ~3 am and~3 pm.

### *2.6 TGO NOMAD*

The NOMAD spectrometer suite aboard the TGO spacecraft combines three channels, covering a spectral range from the UV to the IR (Vandaele et al., 2015). NOMAD can perform solar occultation, nadir, and limb observations. The solar occultation only channel (SO) covers the infrared (2.3–4.3 μm), the second infrared channel (2.3–3.8 μm) can observe in nadir, but also solar occultation and limb viewing geometry (LNO – Limb Nadir and solar Occultation), and the ultraviolet/visible channel (UVIS – UV visible, 200–650 nm) can work in all observation modes. The TGO spacecraft is in a 2-hr precessing orbit that enables NOMAD to observe the day and nightsides of Mars at many local times and latitudes. The majority of observations are for local hours between 8 am and 4 pm. The nominal science phase operations began in MY34 at $L_s$~140° (March 2018). In this work we use retrievals of water vapor abundances from the NOMAD LNO channel (Crismani et al., 2021) during the first year of the mission ($L_s$~140° in MY34 to $L_s$~135° in MY35).

### *2.7 Dust opacity datasets*

For our study, we looked at the three most recent GDSs that occurred during MY25, MY28, and MY34. We have chosen to use dust opacity data retrieved from TES, THEMIS and

MCS observations for these storms. We have selected observations by these particular instruments because they provide good spatial and temporal coverage of the SPR in years with and without GDSs. Martian GDS typically occur between southern spring ($L_s$=180°) and summer ($L_s$=270°), but each dust storm can have vastly different characteristics (Wolkenberg et al., 2020). Figure 2 illustrates evolution of dust opacities in the zonal band between latitudes 40°S and 60°S observed by TES, THEMIS, and MCS during second half of MY24, MY25, MY28 and MY34. TES MY24 observations provide a reference for a typical Mars year without a GDS. The GDSs that occurred in MY25 and MY34 began early in the dust season at $L_s$ ~185°, near the southern vernal equinox. Both became planet encircling storms by $L_s$ ~193°, however their decay phases had significantly different durations. In MY25 the atmospheric dust opacity remained above climatological values until $L_s$ ~275°, while the MY34 storm lasted only until $L_s$~230°– much shorter compared to the events in MY25 and MY28. Meanwhile, the GDS of MY28 began much later in the dusty season with an onset of $L_s$~265° after perihelion during the period of solsticial activity (Wolkenberg et al., 2020). Elevated dust loading was distributed throughout the entire planet as far north as 40°N during this storm. An increase in dust opacities starting on $L_s$=320°–340° in MY34 corresponds to a regional storm ‘C’ typically occurring at this time of Mars year (Kass et al., 2016).

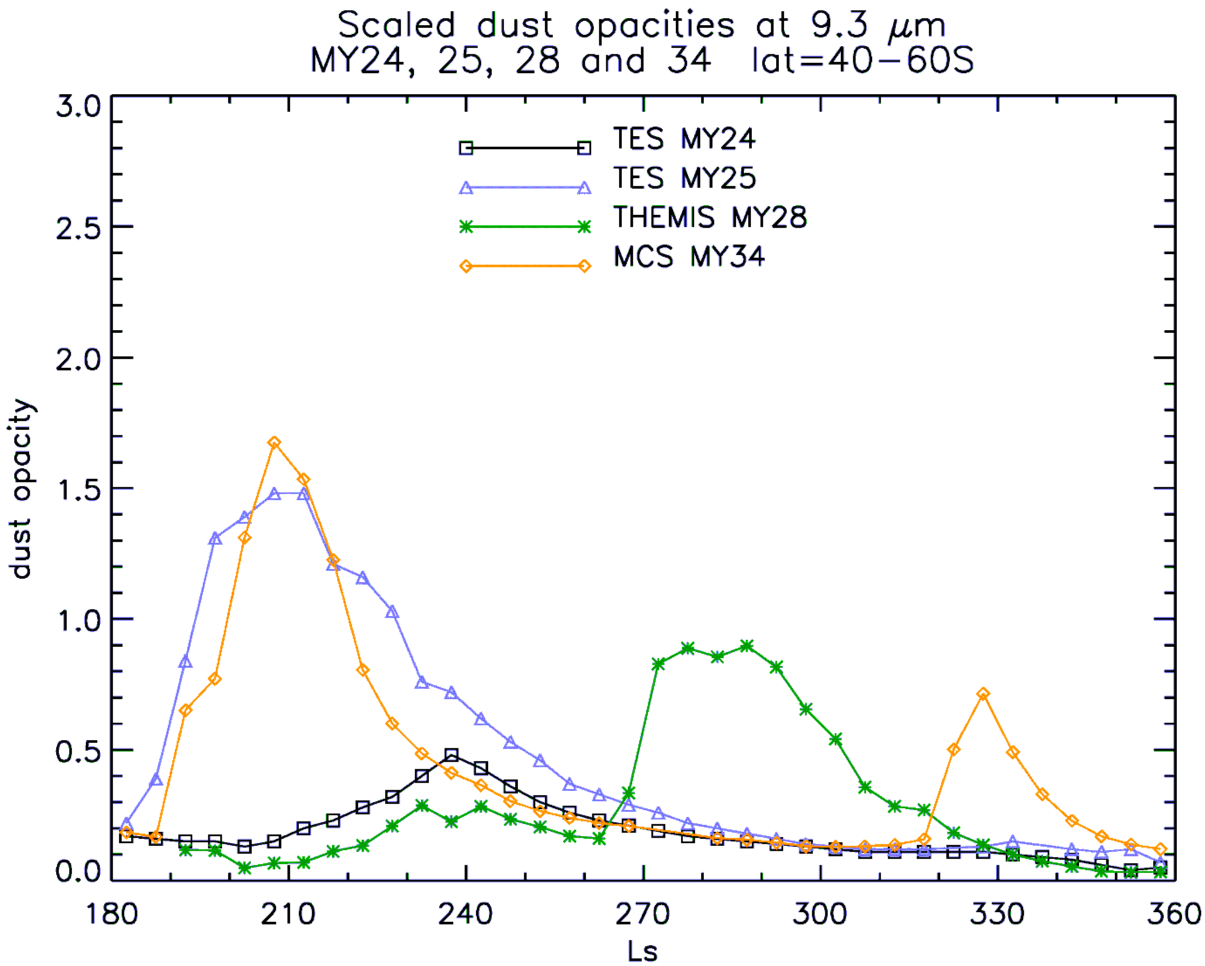


**Figure 2. Zonally averaged surface pressure-scaled dust opacities (at 1075 cm$^{-1}$) in the zonal band 40°S-60°S during years with GDSs: MY25, MY28, MY34. Dust opacities during MY24 illustrate typical variability of dust during southern spring and summer in a year without a GDS. Increased dust opacities around $L_s$=330° in MY34 correspond to a regional dust storm.**

### 2.7.1 MGS TES dust opacity

Dust opacities for MY24 and MY25 were extracted from derived products of re-calibrated TES dataset (Pankine 2020; 2022a; Pankine et al., 2023). These dust opacities were retrieved from TES spectra that were corrected for the presence of a calibration error (Pankine, 2015; 2016). The retrieval algorithm is similar to that used by Smith (2004), but accounts for the presence of radiometric error in the TES spectra (Pankine et al., 2023). This results in a relatively small difference (~5%) between daytime dust opacities used in this work and those derived by

Smith (2004).The retrieval algorithm searches for the best fit to radiances observed in multiple TES spectral channels by iteratively varying dust and water ice opacity, and surface temperature (Smith, 2004). Atmospheric temperatures used in the retrieval are retrieved from TES radiances across the 665 cm$^{-1}$ $CO_2$ absorption band in a separate step (Conrath et al., 2000). TES dust opacities are for wavenumber 1075 cm$^{-1}$.

### 2.7.2 MO THEMIS dust opacity

Dust opacities for MY28 are from the THEMIS dataset that covers MY26–29 (Smith, 2009). The THEMIS dust opacity retrieval algorithm finds the best fit to radiances in THEMIS Bands 3–8 (roughly 830–1250 cm$^{-1}$) by iteratively varying dust and water ice opacities. Atmospheric temperatures used in the retrieval were found in a separate step using observations in THEMIS Band 10 and climatological TES temperatures (Smith, 2009). THEMIS dust opacities are for wavenumber 1075 cm$^{-1}$, similar to TES.

### 2.7.3 MRO MCS dust opacity

Dust opacities for MY29 and MY34 were extracted from the MCS dataset (Kleinböhl et al., 2009). MCS dust opacities are retrieved from radiances in channel A5, centered around 463 cm$^{-1}$ (21.6 μm). For limb retrievals retrieved dust opacity profiles between 10–80 km are extrapolated to the surface. MCS opacities at 463 cm$^{-1}$ were converted to opacities at 1075 cm$^{-1}$ (9.3 μm) for ease of comparison with TES opacities using a conversion factor of 2.2 corresponding to the ratio of extinction coefficients at these wavenumbers for dust particles with radius 1.5 μm (Wolff and Clancy, 2003).

## *2.8 Dust opacity uncertainties*

Typical retrieval errors for daytime dust opacities are ~10% (e.g. Smith 2004; Smith 2009; Kleinböhl et al. 2009). Retrieval errors are likely higher during intense dust storm events, possibly reaching 20% and higher (Smith 2009). Hundreds of individual retrievals are typically averaged to produce the zonal averages used in this work, significantly reducing opacity uncertainty associated with random errors. However, retrieval uncertainties associated with calibration and other systematic errors are not reduced by averaging. During GDS when dust opacities increase above unity at the observing spectral range, dust in the lowest part of the atmosphere is not detectable by orbiting remote sensing instruments, which may lead to an underestimation of opacities by 30–50%. Another potential source of error is the choice of the factor for converting MCS opacities at 463 $cm^{-1}$ to 1075 $cm^{-1}$. We assume effective radius of 1.5 μm for the dust particles corresponding to a conversion factor of 2.2. Figure 2 shows that MCS opacities in MY34 during times outside of strong dust events are consistent with opacities retrieved by TES in MY24 ($L_s$=240°–320°), supporting this choice of conversion factor. During a GDS, larger particles could be lofted into the air, increasing the effective radius of the dust particles population (Wolff and Clancy, 2003). For particles with effective radius of 2 and 3 μm, the conversion factors are 1.9 and 1.5, respectively. Therefore, estimated MCS opacity at 1075 $cm^{-1}$ could be overestimated by ~15–30% during a GDS. In this work, we do not use dust opacity directly in our analysis. We use it to establish the time period when the atmosphere is affected by the dust activity during a GDS. Since large dust particles appear in the atmosphere at the peak of the storm, the uncertainty in the dust opacity that is associated with possible underestimation of dust particle sizes is the largest during the same time. However, this has no effect on the determination of the time period when dust opacities are elevated during a GDS above their typical values. Therefore, the uncertainty of the dust opacity conversion factor has no effect on our analysis.

### *2.9 Water vapor datasets*

The water vapor abundance datasets used in this work are briefly reviewed below.

#### **2.9.1 MGS TES water vapor**

Water vapor abundances for SPR in MY24–25 were retrieved from TES daytime nadir observations (Pankine and Tamppari, 2019). TES vapor abundances were retrieved from the 200–300 $cm^{-1}$ (50–33 μm) spectral region in the TES spectra. Atmospheric temperatures required for the retrieval were retrieved from TES spectra in a separate step (Conrath et al., 2000). Retrievals over low-temperatures regions ($T_{surf}$<240 K), such as recently thawed areas in the SPR and nighttime surfaces, have higher uncertainties than vapor retrievals over warmer surfaces (Smith 2002; 2004).

#### **2.9.2 MRO CRISM water vapor**

We use water vapor abundances retrieved from CRISM nadir spectra at ~3 pm local time from the ~2.6-μm spectral band (Smith et al., 2018) in MY29 for comparison to NOMAD vapor data in MY34 (see discussion in Section 3.3). CRSIM vapor abundances are also available for MY28, and they show behavior similar to SPICAM abundances (Section 2.9.3). In the interest of keeping the paper short, analysis of the GDS in MY28 is based on the SPICAM data only. CRISM water vapor retrievals are run on spectra averaged from 100×100 pixels in the central area of the nadir image. The water vapor ~2.6-μm spectral band is mixed with a strong $CO_2$ band, therefore $CO_2$ and water vapor retrievals are run simultaneously. Spectra with spectral signatures of surface ice are excluded from retrieval. Atmospheric temperatures required for retrieval are taken from TES climatology (Smith, 2004). Atmospheric dust and water ice aerosols affect spectral signatures of gases observed in CRISM spectra and their optical depths are taken from concurrent observations from THEMIS (Smith et al., 2009).

### 2.9.3 MEX SPICAM IR water vapor

Water vapor abundances are retrieved using the ~1.38 μm spectral band (Trokhimovskiy et al., 2015). We use SPICAM daytime retrievals in MY28–29 to compare vapor abundances in the SPR during GDS and non-GDS years. Vapor retrievals were limited to those for local hours between 6 am and 6 pm to minimize effects of possible diurnal variability when comparing to TES vapor abundances (see discussion in Section 2.10). Pressure and temperature profiles required for the retrieval were taken from the Mars Climate Database (MCD, Millour et al., 2009).These profiles were simulated by the Global Circulation Model (GCM) with assimilated TES data. SPICAM IR retrieval accounts for scattering effect of atmospheric aerosols (dust and water ice). Opacities of aerosols were taken from THEMIS (Smith et al., 2009) and interpolated to locations and times of SPICAM IR observations.

### 2.9.4 TGO NOMAD water vapor

NOMAD LNO channel can measure water vapor abundances in the atmosphere of Mars using observations in the 2.3–4.3 μm spectral range (Crismani et al., 2021). We use NOMAD water vapor abundances retrieved from daytime observations during $L_s$=180°–360° in MY34 to study the effects of the GDS in MY34 on the water vapor cycle in the SPR. There were no NOMAD data for $L_s$=180°–360° for years after MY34 to compare with NOMAD MY34 at the time this work was carried out. Therefore, we compare NOMAD abundances during and after the GDS of MY34 to CRISM abundances in MY29 during the same season, and we use NOMAD abundances during $L_s$=0°–135° in MY35 for comparison with CRISM data in MY29 to establish that vapor abundances are similar in the two datasets during times of low atmospheric dust loading. The majority of NOMAD observations in MY34 are for local hours between 8 am and 4 pm. Limiting analysis to local hours of observations in the range from 11 am to 4 pm reduces the number of available data, but does not significantly change the results reported in Section 3.3.

### *2.10 Water vapor abundance uncertainty*

Uncertainty due to random factors in retrieved water vapor abundances are typically below 10–20% for the datasets used in this work. Zonal averaging of many individual retrieval significantly reduces this uncertainty, to the level of a few percent or lower. Systematic uncertainties that are not reduced by averaging could be associated with calibration, choice of environmental parameters, and approach to modeling vapor absorption. Different instruments measure different bands of water (SPCIAM IR: ~1.38 µm; CRISM and NOMAD: ~2.6 µm; TES: ~25–50 µm), and therefore, make different assumptions about modeling the absorption features, aerosols and surface at their respective spectral ranges. These uncertainties are difficult to quantify. Systematic differences between different datasets of water vapor abundances have been noted before (Tschimmel et al., 2008; Fedorova et al., 2010; Pankine, 2022b) and are subject of ongoing debate. To avoid systematic differences, we compare vapor abundances measured by the same instruments. When this is not possible (like in the case of GDS in MY34), and results from different instruments are compared (NOMAD and CRISM), we verify that these instruments retrieve similar vapor abundances during times of low dust loading, and, therefore, there are no systematic differences between these instruments. Different instruments observe water vapor at different local times and detected vapor abundances may differ due to diurnal variability of vapor abundances. Water vapor mixing ratios vary diurnally due to formation of water ice clouds and near-surface fog at night, and due to desorption/adsorption exchange with the subsurface. However, these changes are small and do not noticeably affect column abundances (e.g. Savijarvi et al., 2019). Nevertheless, we limit our analysis to daytime vapor abundances to minimize possible differences associated with vapor diurnal cycle.

## 2.11 *Surface-temperature datasets*

### 2.11.1 MGS TES surface temperatures

Surface temperatures for MY24 and MY25 were extracted from derived products of re-calibrated MGS TES dataset (Pankine 2020; 2022a).These surface temperatures were retrieved from TES spectra corrected for the presence of calibration error and radiometric error (Pankine et al., 2023). These surface temperatures may differ by 1−2 K from the temperatures retrieved by Smith (2004) for surface temperatures above ~240 K. For lower temperatures, the difference could be larger (~10 K), because calibration and radiometric errors effects were larger for observations of low radiances.

### 2.11.2 MRO MCS surface temperatures

Surface temperatures for MY29, MY33 and MY34 were extracted from the MCS dataset (Kleinböhl et al., 2009). For limb observations surface temperature is determined by extrapolating from atmospheric temperature at the lowest level. Similar to dust opacities, MCS surface temperatures are available starting from MY28 $L_s$=330°.

### 2.11.3 MO THEMIS surface temperatures

Surface temperatures for MY28 were extracted from the THEMIS dataset (Smith, 2009). THEMIS surface temperatures are found as part of the retrieval of atmospheric aerosol opacities. THEMIS surface temperatures are available only for daytime (~4 pm to 6 pm) and only for locations with $T_{surf}$ above ~225 K.

## 3. Results

This section presents inter-comparison results between environmental fields observed during GDS years in MY25, MY28 and MY34 and adjacent non-GDS years.

### *3.1 MY25 GDS*

To explore the influence of the MY25 GDS on the water vapor cycle at the SPR, we compare TES observations in MY25 to observations in non-GDS MY24. Figure 3 compares zonally averaged water vapor column abundances and dust opacities during $L_s$=180°–360° in MY25 and MY24. Data for the MY25 dust storm year are shown in red, while MY24 non-dust storm year data are in blue. The GDS of MY25 manifests itself as a sharp rise in the dust opacity in the 40°S–50°S and 50°S–60°S latitudinal bands starting from $L_s$ ~180°. Dust opacity peaks in these bands at Ls~210°. The relative increase in dust opacities in MY25 relative to MY24 decreases from the outermost zonal band of 40°S–50°S to the innermost band of 80°S–90°S as atmospheric dust is unable to penetrate deep into the polar atmosphere. Dust opacities in MY25 remain higher than in MY24 in all zonal bands until $L_s$~235°, except in the outermost band, where elevated opacities in MY25 are observed for much longer – until $L_s$~290°. In response to the GDS, the vapor column abundances in MY25 decrease compared to MY24. The earliest time vapor abundances can be retrieved in the 40°S–60°S zonal bands following the start of the storm in MY25 are at $L_s$=220°–225°. In the 60°S–70°S zonal band vapor abundances do not appear to deviate from MY24 abundances until $L_s$~210°. After that $L_s$ the observed dust opacity in the 50°S–70°S zonal bands is decreasing from its peak value until it returns to typical values at $L_s$~230°, but the depletion in water vapor column abundances persist late into the Martian year, until $L_s$~310°.

Moving further south, the delay in vapor column depletion during GDS year is even more noticeable in the 70°S–80°S and 80°S–90°S latitudinal bands, where the water vapor column abundances during the dust storm year are similar to abundances in MY24 all the way until $L_s$~250°– well into the decay phase of the MY25 dust storm. Lower vapor abundances in MY25 are observed until $L_s$~310°, long after dust opacity levels in MY25 have returned to MY24 levels.

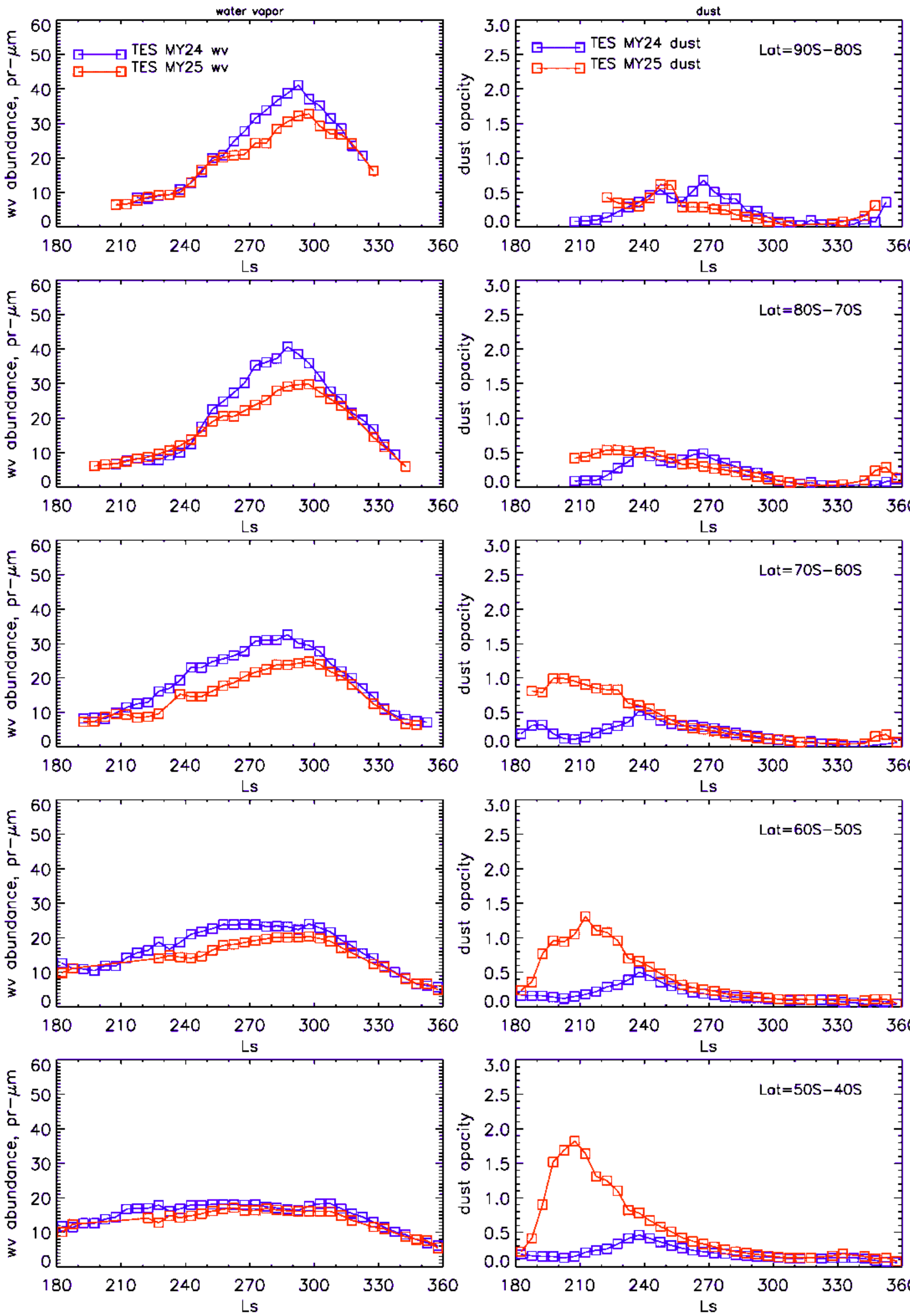


**Figure 3. TES daytime water vapor column abundances (left) and scaled dust opacities (right) during $L_s$=180°-360° in MY24 (blue) and MY25 (red).**

The increase in atmospheric opacity during the peak of the MY25 storm leads to daytime surface temperatures being significantly cooler than during MY24 (middle row in Figure 4). The decrease in daytime temperatures reflects reduced insolation during the GDS. Following the storm ($L_s$~275°, bottom row in Figure 4), surface temperatures return to pre-storm levels, however water vapor remain lower than MY24 levels.

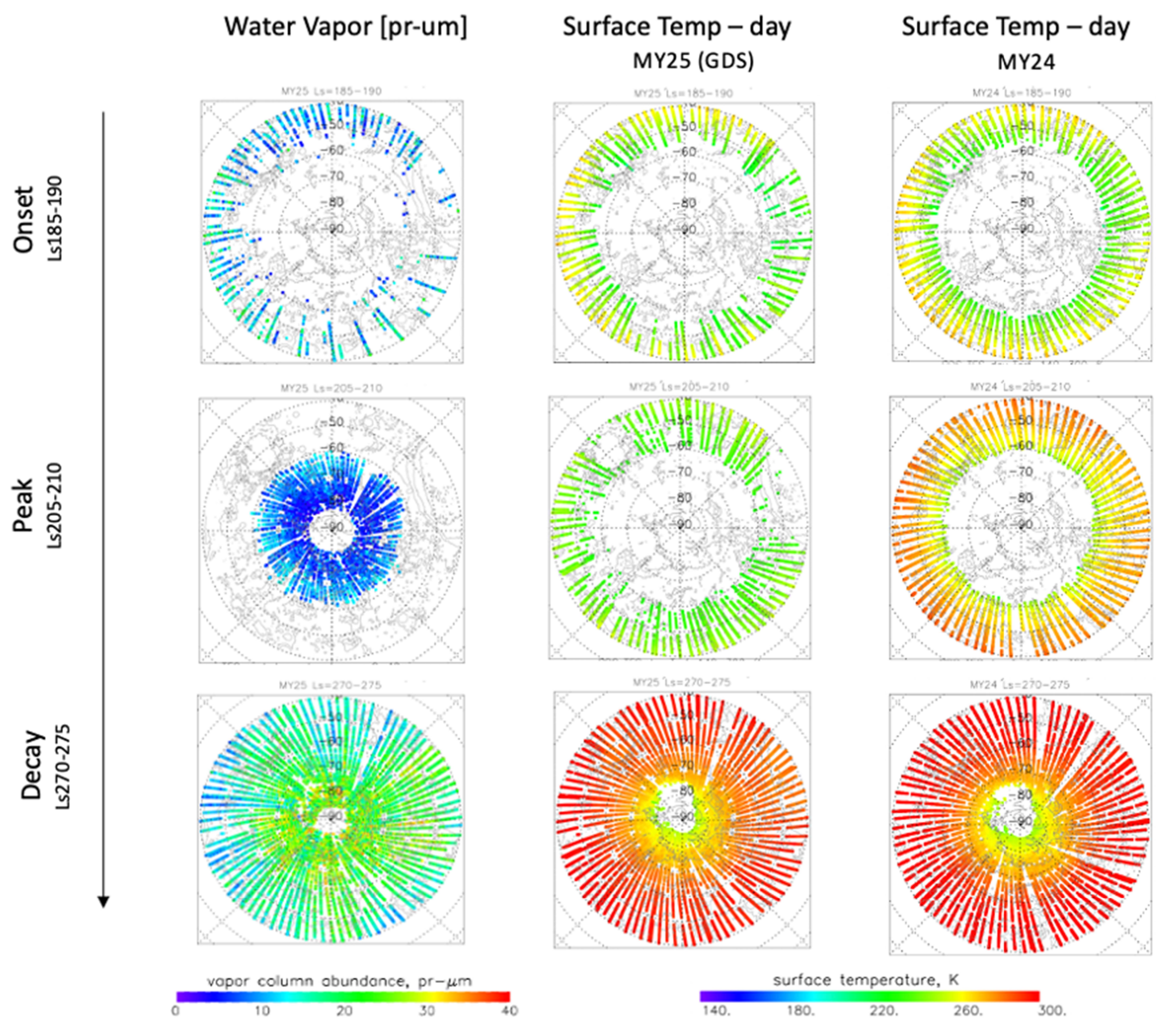


**Figure 4. Polar plots of MGS TES water vapor in MY25 (left), and MGS TES daytime surface temperatures in MY25 (middle) and MY24 (right) in the SPR during $L_s$=185°-190° (top), 205°-210° (middle) and 270°-275° (bottom).**

Figure 5 shows the behavior of the MGS TES daytime and nighttime surface temperatures $T_{surf}$ in the SPR during the seconds half of MY24 and MY25. Daytime surface temperatures during the dust storm decrease in the zonal bands between 40°S and 70°S. This decrease is in response to a decrease in insolation due to increased atmospheric opacity. The dust storm has very little effect on the daytime $T_{surf}$ poleward from 70°S, because the sun is still low over horizon during most of the storm ($L_s$=210°–240°) and does not provide significant heating to the ground. This can be seen in the behavior of the $T_{surf}$ during MY24, where the temperature does not begin to increase above ~160 K until after $L_s$~235° and ~250° in the 70°S–80°S and 80°S–90°S bands, respectively. Parts of these zonal bands are still covered by the seasonal $CO_2$ frost during this time, but only areas that are free from ice are used to calculate $T_{surf}$ (see Section 2.11).

Nighttime surface temperatures during the MY25 dust storm increase in the zonal bands between 40°S and 60°S (Figure 5). The increase is in response to relatively larger downwelling IR radiation at nighttime caused by enhanced opacity. The effect of the storm on nighttime $T_{surf}$ in the zonal 60°S–70°S is very small (due to low temperatures) and cannot be seen in Figure 5. Retrievals of nighttime $T_{surf}$ are not available in the zonal bands south of 70°S until $L_s$~225°–235° when atmospheric dust opacities in MY25 and MY24 are very similar. No difference is observed between nighttime $T_{surf}$ in these zonal bands.

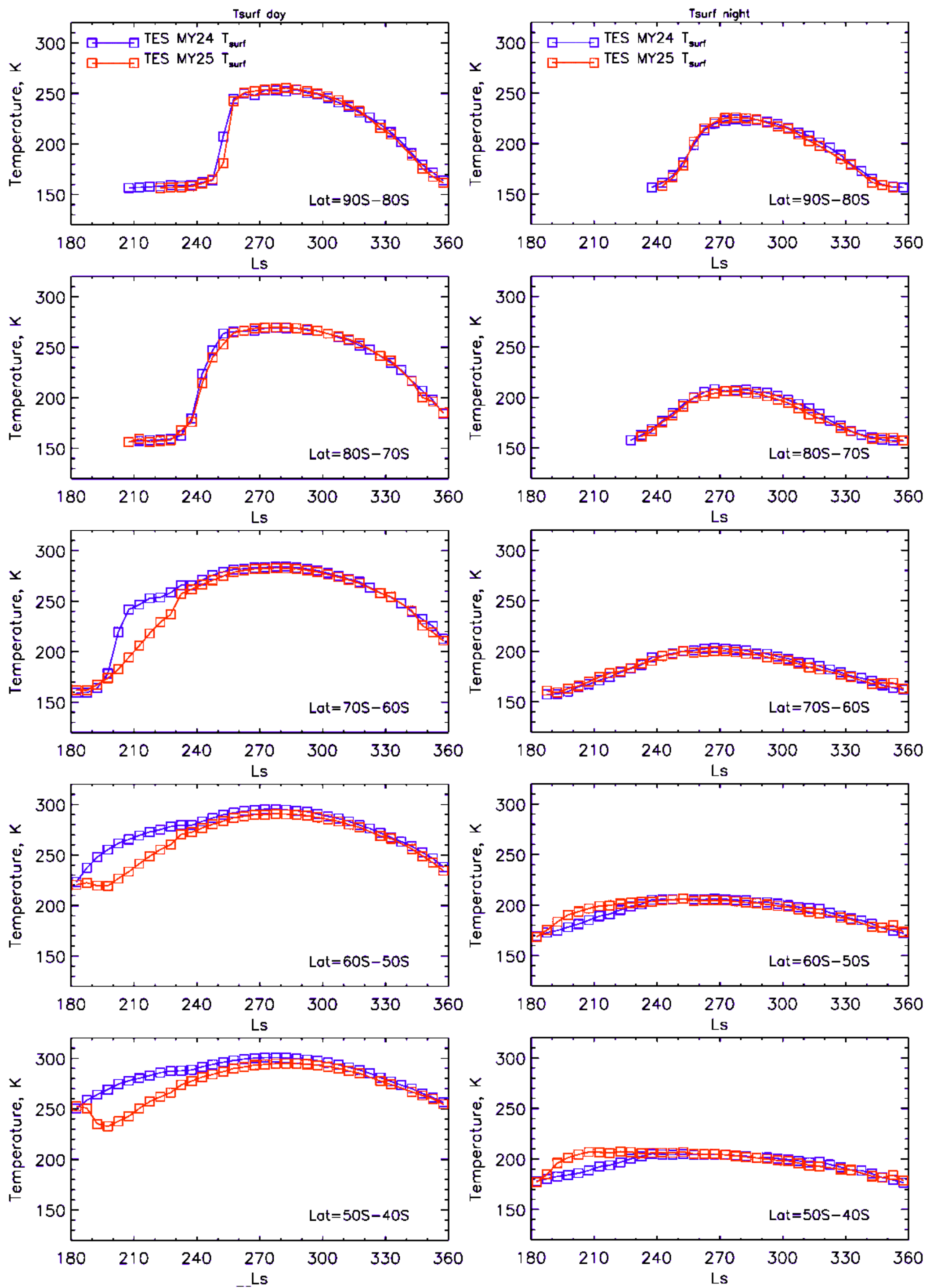


**Figure 5. MGS TES daytime (left) and nighttime (right) surface temperatures in the SPR during MY24 (blue) and MY25 (red).**

### *3.2 MY28 GDS*

Figure 6 compares water vapor abundances and dust opacities during MY28 and MY29. For the comparison between adjacent years MY28 (GDS) and MY29 (non-GDS), we use water vapor column abundances from Mars Express SPICAM (Section 2.9.3), and dust opacities from THEMIS for MY28 (Section 2.7.2) and MCS for MY29 (Section 2.7.3). MCS data are not available for MY28, thus necessitating the use of two different datasets for dust opacity data. THEMIS data typically have poorer latitudinal coverage than MCS data, therefore we used MCS rather than THEMIS data for MY29. Water vapor abundances in the SPR in MY28 and MY29 are also available from CRISM observations, and they show similar behavior as the abundances retrieved from SPICAM data. Only SPICAM data are shown below to keep the paper short.

The GDS of MY28 began around southern summer solstice at $L_s$~265°. Dust opacities can be seen increasing sharply at latitudes between 40°S –70°S at this time (Figure 6). In the 40°S –60°S bands, dust opacity did not return to pre-storm levels until $L_s$~310°–315°. Dust opacities did not noticeably increase in the 70°S –90°S latitudinal bands suggesting that southward transport of dust was limited during the MY28 GDS.

The vapor column in zonal bands between 40°S–90°S is observed to respond nearly immediately after the sharp rise in dust opacities in the outer (40°S–60°S) bands at $L_s$~265°. Even at high southern latitudes where the dust does not penetrate as far south towards the poles, the relative change in vapor column is significant, decreasing from 30 pr-μm during $L_s$~280°–300° in MY29, to only 10 pr-μm during the same time period in MY28 GDS year (Figure 6). Water vapor abundances in MY28 continue to be lower than in MY29 until $L_s$~320°–330°. Water abundances remain lower than in MY29 even after dust opacities return to pre-storm levels after $L_s$~310°. Areas south of 70°S are relatively clear of dust during the MY28 storm. However, water abundances over these latitudes are noticeably lower than during the same period in MY29 ($L_s$=270°–310°).

In MY29 when no GDS was present, vapor abundances generally increase during southern spring and early summer ($L_s$=180°–280°), reflecting the southward transport of vapor by atmospheric circulation and sublimation of seasonal surface frost (Figure 6). A temporary decrease in abundances at $L_s$=230°–255° coincides with a regional dust storm 'B' (Kass et al., 2016). Unlike after the GDS of MY28, vapor abundances quickly increase to their pre-storm level after the end of the regional storm. Vapor abundances reach their maximum values (~30 pr-μm) at latitudes 70°S–90°S at $L_s$~280°–295° after the seasonal polar cap completely disappears.

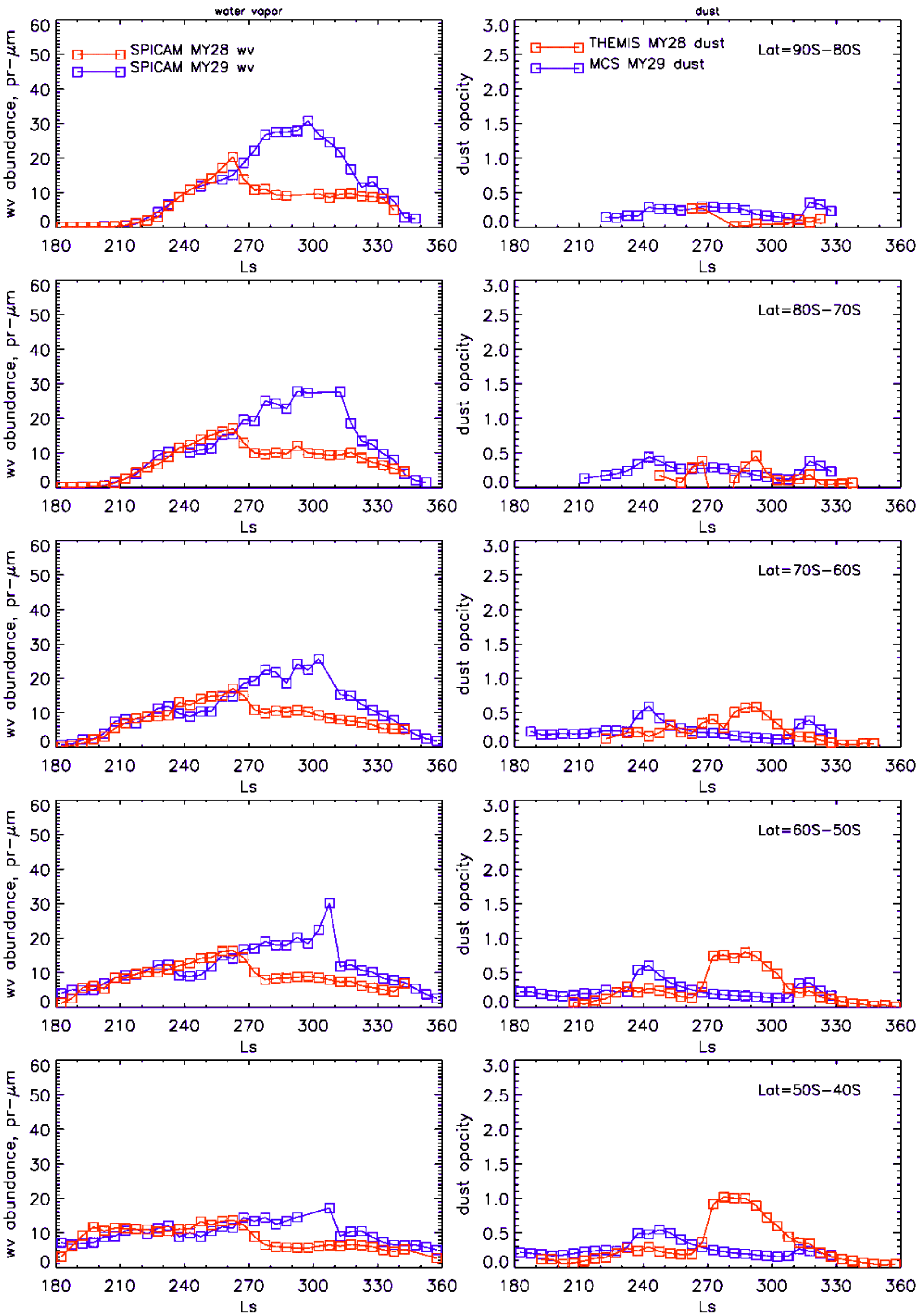


**Figure 6. (Left) SPICAM IR daytime water vapor column abundances in MY28 (red) and 29 (blue). (Right) THEMIS MY28 (red) and MCS MY29 (blue) dust opacities during $L_s$=180°–360°.**

Polar plots show spatial variability of dust before, during, and after the MY28 GDS, and the coincident changes in the polar ice cap extent during this season.

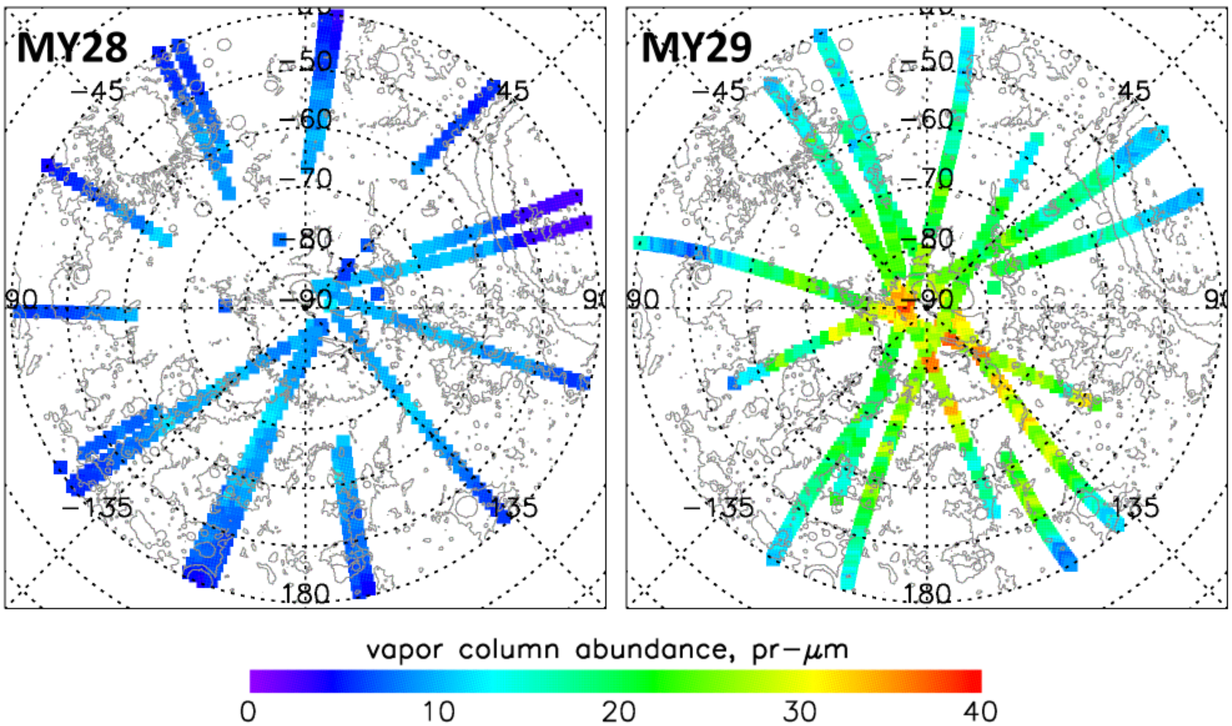


**Figure 7. Polar map of SPICAM IR scaled water vapor abundances at $L_s$~280°–290° in MY28 GDS year (left), and in MY29 non-GDS year (right).**

Comparison of water vapor abundances observed by SPICAM IR in MY28 vs. MY29 shows a strong response in the water cycle during the MY28 GDS (Figure 6, Figure 7). In particular, water vapor abundances at all latitudes in the SPR declined sharply at the onset of the MY28 GDS ($L_s$~260°) and remained at lower values until $L_s$~320°–330° when compared to vapor abundances during a nominal year without a GDS (e.g., MY29). Polar plots of vapor column abundances in the SPR at $L_s$=280°–290° in MY28 and MY29 in Figure 7 illustrate the difference between years with and without a GDS. The suppressed vapor abundances over the SPR were observed even when the dust opacity decreased to pre-storm levels.

Figure 8 compares daytime surface temperatures in the SPR in MY28 and MY29. Observations in MY28 are by THEMIS, because MCS observations in MY28 started only after $L_s$~330°. No nighttime THEMIS observations are available. Daytime THEMIS surface temperatures are for local times that vary between 4 pm and 6 pm, while MCS observations are for 3 pm. This difference in local times of observations may be responsible for some of the difference between THEMIS and MCS surface temperatures in Figure 8. However, the decrease in THEMIS daytime $T_{surf}$ relative to MCS temperatures in the zonal bands north of 70°S during $L_s$=270°–310° correlates with the increase in the atmospheric dust opacities and likely represents the response to decreased insolation.

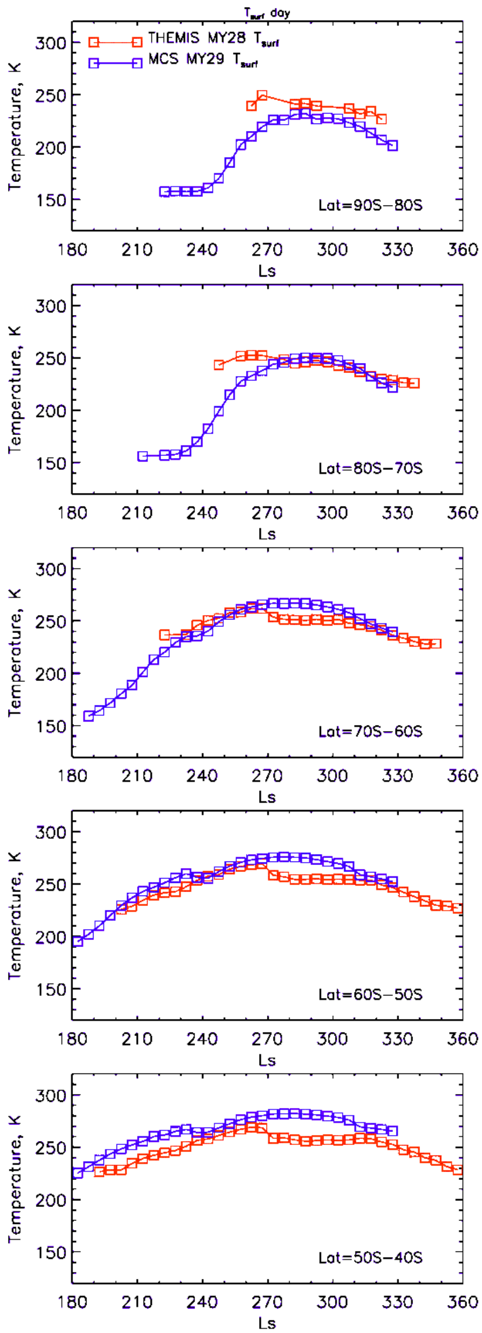


**Figure 8. Comparison of daytime surface temperatures in the SPR during THEMIS MY28 (red) and MCS MY29 (blue).**

### *3.3 MY34 GDS*

For the GDS in MY34, we use water vapor column abundances retrieved by TGO NOMAD. At the time this study was carried out, retrievals of NOMAD water vapor abundances were only available for the time interval from $L_s$~150° in MY34 to $L_s$~135° in MY35 (as a supplement to Crismani et al., 2021). Therefore, NOMAD vapor abundances during the second half of MY34 could not be compared to other NOMAD observations of the same season in a different year. We use CRISM observations during non-GDS MY29 as the reference observations for comparison with NOMAD MY34. There are two reasons for selecting CRISM observations for comparison with NOMAD. First, both instruments use water vapor absorption near 2.6 μm to retrieve atmospheric abundances, which likely reduce possible uncertainties that could be associated with the usage of absorption models for different spectral ranges. Second, NOMAD and CRISM retrieved abundances compare well for seasons with low atmospheric dust levels (i.e., $L_s$=0°−180°) between different years. To compare CRISM and NOMAD vapor abundances during different Mars years, individual retrievals were zonally averaged in zonal bands 4° wide and in $L_s$ intervals 5° wide. NOMAD retrievals with local times between 8 am and 4 pm were used. Local times of CRISM observations are ~3 pm. Daytime vapor abundances are not expected to be significantly affected by the diurnal cycle of water vapor (see discussion in Section 2.10), therefore, the difference in local hours of observations between the two datasets should not affect the comparison. Figure 9 shows the comparison between averaged CRSIM and NOMAD abundances in latitude-$L_s$ bins during $L_s$=0°−135° in MY29 and MY35 (orange symbols) and during $L_s$=150°−360° in MY29 and MY34 (blue symbols). The solid line indicates a one-to-one correspondence between CRISM and NOMAD abundances, while the dashed line corresponds to NOMAD abundances being a factor of two lower than CRISM abundances.

$L_s$=0°−150° is typically the low dust period of the Martian annual dust cycle (Smith 2004; 2008). Figure 9 shows that during this time period in MY29 and MY35, NOMAD vapor abundances show a high degree of similarity with CRISM abundances, falling close to the one-to-one correspondence line, except for when NOMAD abundances are low (~1–7 pr-μm), which are ~3–4 pr-μm lower than the CRISM observations. In contrast, the NOMAD abundances retrieved during the second half of MY34, which includes the appearance of the GDS, are seen to be consistently lower than CRSIM abundances, reflecting the effects of dust loading on the water cycle during and after the GDS.

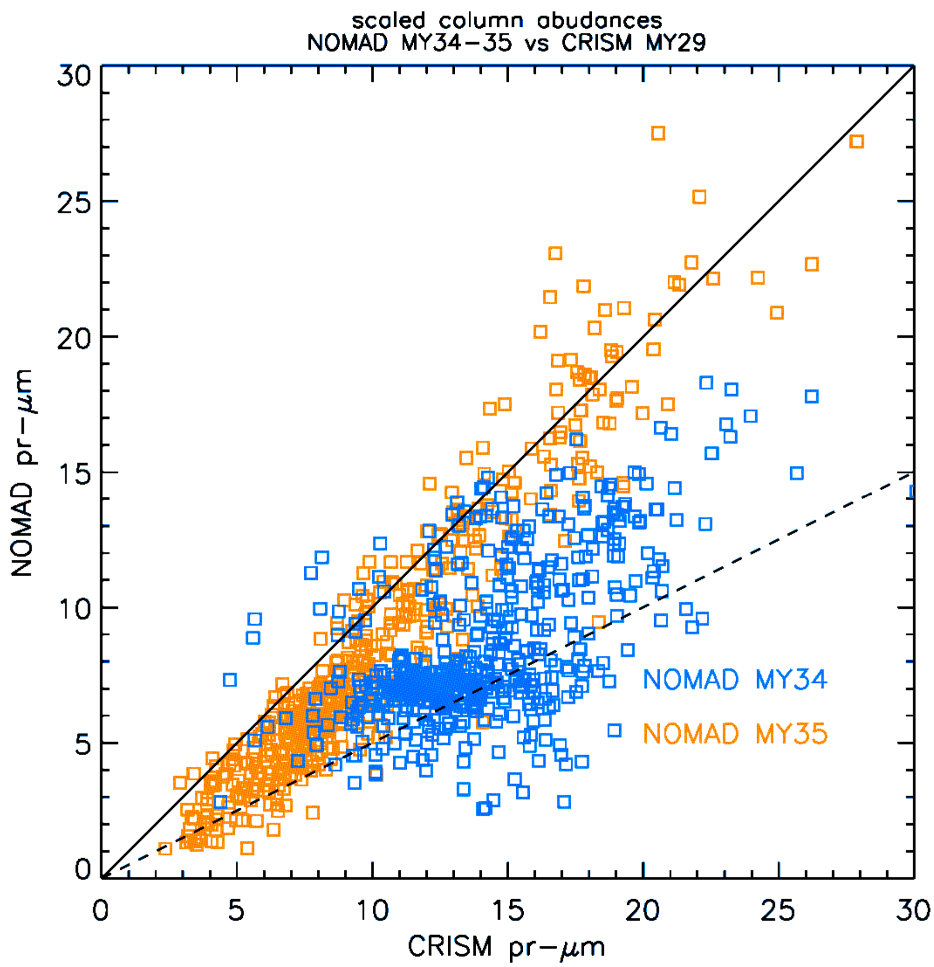


**Figure 9. Comparison of the averaged NOMAD and CRISM water vapor abundances in the same latitude-$L_s$ bins during $L_s$=150°-360° in MY29 and MY34 (blue), and $L_s$=0°–135° in MY29 and MY35 (orange).**

The effects of the MY34 GDS on the vapor cycle in different zonal bands in the SPR are illustrated in more detail in Figure 10. Panels in the left column of Figure 10 compare zonally averaged water vapor abundances derived from CRISM data in MY29 and NOMAD data in

MY34 during $L_s$=180°−360°, for different latitudinal bands. Zonally averaged scaled MCS dust abundances in the SPR in MY29 and MY34 are shown in the right column in Figure 10 for the same latitudinal bands. The GDS of MY34 manifests itself as an increase of dust opacities during $L_s$=185°−240° at latitudes north of 70°S. The highest opacities are observed at $L_s$~210°. There were no valid NOMAD water vapor data in the innermost zonal band of 80°S−90°S, therefore only CRISM vapor data appear in this band. In the other zonal bands, NOMAD vapor abundances appear systematically lower than CRISM abundances during and after the GDS. CRISM abundances are typically higher than NOMAD abundances by ~5−10 μm, except at $L_s$~245°−250° at latitudes 60°S−80°S when this difference decreases to 2−4 μm. We attribute this systematic difference between vapor abundances in the year with and without the GDS to effects of the GDS.

Figure 11 provides a comparison between daytime (left column) and nighttime (right column) surface temperatures observed by MCS in MY29 and MY34. During the MY34 GDS, MCS daytime surface temperatures decrease by several degrees at latitudes equatorward of 70°S. The decrease is associated with the increase in atmospheric opacity decreasing insolation. The difference between daytime surface temperatures at latitudes south of 70°S between MY29 and MY34 is very small because atmospheric opacities remain low at these latitudes during the GDS. The recently thawed ground is still very cold ($T_{surf}$~160 K) and is slow to respond to changes in insolation, and insolation levels are low at these high southern latitudes during early spring. Nighttime surface temperatures increase at latitudes north of 70°S because of the higher atmospheric opacities that reduce surface heat loss at night. Similar to daytime temperatures, nighttime temperatures show little change at latitudes poleward of 70°S for similar reasons.

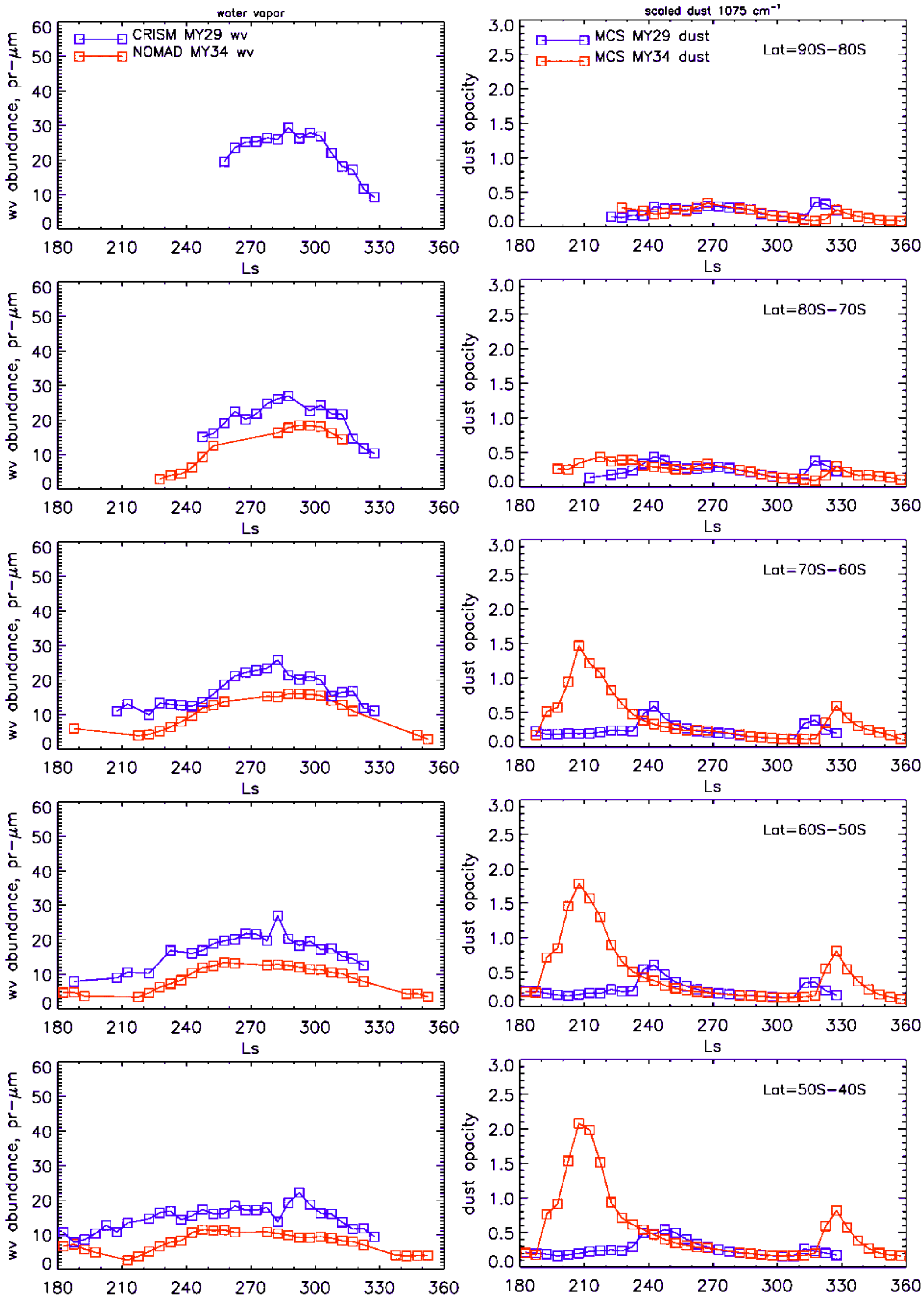


**Figure 10. CRISM and NOMAD water vapor column abundances in MY29 and MY34, respectively (left); MCS MY29 and MY34 dust opacities scaled to 1075 cm$^{-1}$ (right) during $L_s$=180°–360°.**

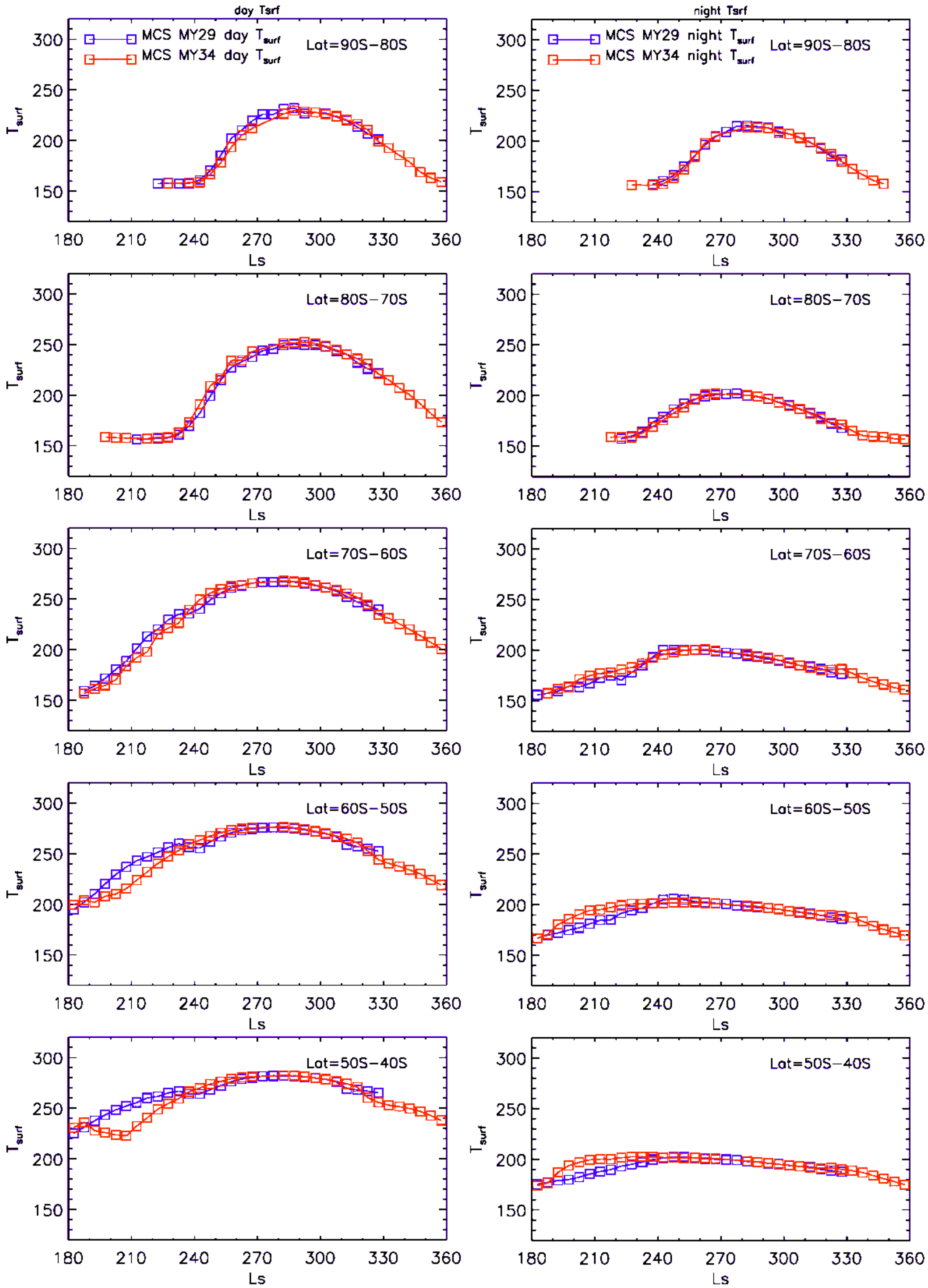


**Figure 11. MCS daytime (left) and nighttime (right) surface temperatures in the SPR during MY29 (red) and MY34 (blue).**

### *3.4 Results from all three Dust Storms*

For all three GDSs that occurred in MY25, MY28, and MY34, water vapor column abundances remain depleted after dust opacities have returned to their climatological values. During the MY25 storm, the decrease in abundances is clearly observed ~50°−70° of $L_s$ after the start of the storm and its magnitude is ~5−10 pr-μm, increasing closer to the South Pole. During the MY28 and MY34 storms, the vapor depletion is observed simultaneously with the onset of elevated dust loading at the start of the GDS in all zonal bands within the SPR. The magnitude of abundance decrease during the GDS of MY28 is ~10–20 pr-μm, increasing towards the South Pole. In MY34 the magnitude of vapor decrease is ~10 pr-μm in all zonal bands. Surface temperatures in the SPR respond to increased dust opacities by decreasing during the day and increasing at night, when compared to same season in years without a GDS. The response of the surface temperatures (day and night) to the increased atmospheric opacity is the weakest south of 70°S latitude in all GDS years analyzed in this work.

## 4. Discussion

All GDSs explored in this study show a decrease in SPR vapor abundances following an increase in dust opacities. This decrease in abundances cannot be attributed to the inability of the orbiting remote instruments to detect atmospheric vapor in the lower atmosphere during times of high atmospheric opacity, because it continues to be observed even after dust opacities return to climatological levels. This decrease in vapor could be interpreted as a response to changes in the atmospheric transport or to changes in surface-atmosphere vapor exchange, as proposed in Pankine and Tamppari (2019). According to the GCM simulations of water vapor transport in the Martian atmosphere in years without a GDS (Steele et al., 2014; Navarro et al., 2014), vapor is concentrated in the equatorial and tropical lower atmosphere at the start of southern spring ($L_s$=180°). In the southern hemisphere, stationary waves transport vapor from the tropics into the southern extra-tropics. By $L_s$=225°, water vapor abundances increase above southern mid-latitudes and poleward transport by stationary waves continues, while vapor released from the sublimating southern seasonal cap is transported from the south pole to mid-latitudes. At the start of the southern summer at $L_s$=270° most of the water vapor is found in the atmosphere above the SPR, with the poleward transport by mean meridional circulation still strong in mid-latitudes. Disruption of this circulation pattern by a GDS at any time during southern spring may cause a net decrease in the vapor transport into the SPR, resulting in a decrease in abundances following the storm. On the other hand, changes to surface temperatures during a GDS may decrease sublimation rates of water ice in the soil pores or vapor desorption rates, also leading to decreased abundances.

All analyzed GDS areas poleward from 70°S exhibit a decrease in vapor abundances during or following the storm even though dust opacities there remain relatively low. This suggests that the decrease in vapor at these latitudes is related to the atmospheric transport rather than to the vapor exchange with the surface. The observed dust opacities remain low near the South Pole during GDS, which is also consistent with weak poleward atmospheric transport from mid-latitudes during this season.

The timing of the water vapor decrease differs across the three storms – the GDS of MY25 shows a delay in a vapor cycle response to increased atmospheric opacities, while during the GDS of MY28 and MY34 the decrease in vapor is coincident with the increase in opacities. Even though the GDS of MY25 and MY34 started at approximately the same time of year ($L_s$~180°–190°), the timing when vapor decreased in different zonal bands was different. The reason for this behavior is unclear. It could be that the $L_s$ date of the GDS is just one of a number of possible factors affecting the response of the water cycle to the dust storm.

The role of atmospheric transport in the observed decrease in vapor abundance in the SPR following a GDS is supported by the NOMAD observation of water vapor vertical distribution during GDS of MY34 (Aoki et al., 2019). In that work, vapor abundances observed by NOMAD during and after the GDS of MY34 were compared to the distribution of vapor simulated by GCM for a non-GDS year. Observed abundances increased at altitudes between 40–100 km in the equatorial region and mid-latitudes in both hemispheres after the onset of the GDS at $L_s$~190°. As the storm developed, abundances decreased at altitudes below 40 km in the equatorial region and mid-latitudes in both hemispheres at $L_s$=210°–215°. This dramatic change in the distribution of water vapor is also supported by the GCM modeling by Holmes et al. (2022). Holmes et al. (2022) simulated water vapor distribution in the atmosphere during the MY34 GDS using a general circulation model and assimilation of observations of temperature, dust, and water vapor from TGO NOMAD and ACS spectrometer suites (Korablev et al., 2018), and from MRO MCS. Simulations showed that vapor moved to altitudes above 40 km during the storm. This redistribution of vapor in the equatorial region and mid-latitudes could explain the observed reduction in vapor abundances in the SPR: the lower atmosphere vapor at mid-latitudes is no longer available for transport to the SPR, which leads to the observed decrease in abundances there following the GDS.

The above discussion supports the idea that changes in atmospheric transport contribute to the decrease in vapor abundances in the SPR following a GDS. However, the role of surface-atmosphere exchange cannot be conclusively excluded. Modeling the changes in the vapor desorption rates is a subject of future investigation.

The Martian water vapor cycle response to a GDS can be compared to the response to a smaller dust storm event. There were two regional dust storms among the years of observations explored in this work: in MY29 during $L_s$=230°‒255° and in MY34 during $L_s$=320°‒350°. In MY29 the regional dust storm caused a decrease of 2‒3 μm in the water vapor abundances at latitudes 40°S‒80°S (Figure 6). However, this decrease in vapor abundances was short lived compared to the GDS effect, and abundances increased with the decreasing dust opacities. A larger regional dust storm started at $L_s$~320° in MY34 (Figure 2, Figure 10). NOMAD coverage of the southern hemisphere at the end of MY34 was poor and vapor abundance retrievals are only available for latitudes 40°S‒60°S during the decay phase of the storm (after $L_s$~335°‒340°) (Crismani et al., 2021). At the start of the regional storm, water vapor abundances were already depleted from the GDS earlier in the season and the late southern summer season of the MY34 regional storm is characterized by low vapor abundances (Smith, 2004; 2008). Therefore, the possible effect of the regional storm on the water cycle cannot be conclusively identified. The relatively small effect of the regional storms on the vapor abundances in the SPR could be due to their short duration and smaller areal extent, which do not sufficiently affect atmospheric transport and surface thermal balance.

## 5. Conclusions

We have analyzed the behavior of atmospheric water vapor at the Martian Southern Polar Region (SPR) during the global dust storm (GDS) years in MY25, MY28 and MY34 using data collected by MGS TES, MEX SPICAM, TGO NOMAD, MRO CRISM and MRO MCS. For all studied storm years, water vapor column abundances decreased by ~10 pr-μm following the GDS, when compared to years without a GDS. We speculate that the decrease in vapor abundances follows the redistribution of water vapor in the atmosphere during the storm, where vapor elevated to higher altitudes in the mid-latitudes becomes effectively removed from the poleward transport, leading to vapor depletion at the SPR.

## 6. Data Availability Statement

The data used in this research can be downloaded from Mendeley Data (https://data.mendeley.com/datasets/mk4bs7v9x9/1) (Pankine, 2023).

## 7. Acknowledgement

Part of this research was carried out at the Jet Propulsion Laboratory, California Institute of Technology (JPL), under a contract with the National Aeronautics and Space Administration (80NM0018D0004). Part of the research was carried out at the Space Science Institute under subcontract 1670135 from Jet Propulsion Laboratory, California Institute of Technology.

## 8. References

Aoki, S., Vandaele, A.C., Daerden, F., Villanueva, G.L., Liuzzi, G., Thomas, I.R., Erwin, J.T., Trompet, L., Robert, S., Neary, L. and Viscardy, S., 2019. Water vapor vertical profiles on Mars in dust storms observed by TGO/NOMAD. J. Geophys. Res.: Planets, 124(12), pp.3482-3497.

Banfield, D., Stern, J., Davila, A., Johnson, S.S., Brain, D., Wordsworth, R., Horgan, B., Williams, R.M., Niles, P., Rucker, M. and Watts, K., 2020. Mars science goals, objectives, investigations, and priorities: 2020 version. Mars Exploration Program Analysis Group (MEPAG).

Brown, A. J., Piqueux, S., and Titus, T. N., 2014. Interannual observations and quantification of summertime $H_2O$ ice deposition on the Martian $CO_2$ ice south polar cap. Earth Planet. Sci. Lett., 406, 102–109. https://doi.org/10.1016/j.epsl.2014.08.039.

Chaffin, M.S., Chaufray, J.Y., Stewart, I., Montmessin, F., Schneider, N.M., and Bertaux, J.L., 2014. Unexpected variability of Martian hydrogen escape. Geophys. Res. Lett., 41(2), 314–320. https://doi.org/10.1002/2013GL058578

Chaffin, M.S., Deighan, J., Schneider, N.M., and Stewart, A.I.F., 2017. Elevated atmospheric escape of atomic hydrogen from Mars induced by high-Altitude water. Nat. Geosci., 10(3), 174–178. https://doi.org/10.1038/ngeo2887

Conrath, B.J., Pearl, J.C., Smith, M.D., Maguire, W.C., Christensen, P.R., Dason, S., and Kaelberer, M. S., 2000. Mars Global Surveyor Thermal Emission Spectrometer (TES) observations: Atmospheric temperatures during aerobraking and science phasing. J. Geophys. Res.,105(E4), 9509-9519.

Crismani, M.M.J., Villanueva, G.L., Liuzzi, G., Smith, M.D., Knutsen, E.W., Daerden, F., Neary, L., Mumma, M.J., Aoki, S., Trompet, L. and Thomas, I.R., 2021. A global and seasonal perspective of martian water vapor from ExoMars/NOMAD. J. Geophys. Res.: Planets, 126(11), p.e2021JE006878

Christensen, P.R., and 25 colleagues, 2001. Mars Global Surveyor Thermal Emission Spectrometer experiment: Investigation description and surface science results. J. Geophys. Res., 106, 23823–23871.

Christensen, P.R., Jakosky, B.M., Kieffer, H.H., Malin, M.C., McSween, H.Y., Nealson, K., Mehall, G.L., Silverman, S.H., Ferry, S., Caplinger, M. and Ravine, M., 2004. The thermal emission imaging system (THEMIS) for the Mars 2001 Odyssey Mission. Space Sci. Rev., 110, pp.85-130.

Fedorova, A.A., Trokhimovsky, S., Korablev, O. and Montmessin, F., 2010. Viking observation of water vapor on Mars: Revision from up-to-date spectroscopy and atmospheric models. Icarus, 208(1), pp.156-164.

Fedorova, A. A., and 21 co-author, 2020. Stormy water on Mars: The distribution and saturation of atmospheric water during the dusty season. Science, 367(6475), 297–300. https://doi.org/10.1126/science.aay9522

Giuranna, M., Wolkenberg, P., Grassi, D., Aronica, A., Aoki, S., Scaccabarozzi, D., Saggin, B. and Formisano, V., 2021. The current weather and climate of Mars: 12 years of atmospheric monitoring by the Planetary Fourier Spectrometer on Mars Express. Icarus, 353, p.113406.

Guzewich, S.D., Lemmon, M., Smith, C.L., Martínez, G., de Vicente-Retortillo, Á., Newman, C.E., Baker, M., Campbell, C., Cooper, B., Gómez-Elvira, J. and Harri, A.M., 2019. Mars Science Laboratory observations of the 2018/Mars year 34 global dust storm. Geophysical Research Letters, 46(1), pp.71-79.

Haberle, R. M., and Jakosky, B. M., 1990. Sublimation and transport of water from the north residual polar cap on Mars. J. Geophys. Res., 95(B2), 1423. https://doi.org/10.1029/jb095ib02p01423

Haberle, R.M., Clancy, R.T., Forget, F., Smith, M.D. and Zurek, R.W. eds., 2017. The atmosphere and climate of Mars. Cambridge University Press.

Heavens, N.G., Kleinböhl, A., Chaffin, M.S., Halekas, J.S., Kass, D.M., Hayne, P.O., McCleese, D.J., Piqueux, S., Shirley, J.H., and Schofield, J.T., 2018. Hydrogen escape from Mars enhanced by deep convection in dust storms. Nature Astronomy, 2(2), 126–132. https://doi.org/10.1038/s41550-017-0353-4

Holmes, J.A., Lewis, S.R., Patel, M.R., Alday, J., Aoki, S., Liuzzi, G., Villanueva, G.L., Crismani, M.M.J., Fedorova, A.A., Olsen, K.S. and Kass, D.M., 2022. Global variations in water vapor and saturation state throughout the Mars Year 34 dusty season. J. Geophys. Res.: Planets, 127(10), p.e2022JE007203.

Jakosky, B. M. ,1983. The role of seasonal reservoirs in the Mars water cycle. I. Seasonal exchange of water with the regolith. Icarus, 55(1), 1–18. https://doi.org/10.1016/0019-1035(83)90046-5

Kass, D.M., Kleinböhl, A., McCleese, D.J., Schofield, J.T. and Smith, M.D., 2016. Interannual similarity in the Martian atmosphere during the dust storm season. Geophys. Res. Lett., 43(12), pp.6111-6118.

Kleinböhl, A., Schofield, J.T., Kass, D.M., Abdou, W.A., Backus, C.R., Sen, B., Shirley, J.H., Lawson, W.G., Richardson, M.I., Taylor, F.W. and Teanby, N.A., 2009. Mars Climate Sounder limb profile retrieval of atmospheric temperature, pressure, and dust and water ice opacity. J. Geophys. Res.: Planets, 114(E10).

Korablev, O., Bertaux, J.L., Fedorova, A., Fonteyn, D., Stepanov, A., Kalinnikov, Y., Kiselev, A., Grigoriev, A., Jegoulev, V., Perrier, S. and Dimarellis, E., 2006. SPICAM IR acousto-optic spectrometer experiment on Mars Express. J. Geophys. Res.: Planets, 111(E9).

Korablev, O., Montmessin, F., Trokhimovskiy, A., Fedorova, A.A., Shakun, A.V., Grigoriev, A.V., Moshkin, B.E., Ignatiev, N.I., Forget, F., Lefèvre, F. and Anufreychik, K., 2018. The Atmospheric Chemistry Suite (ACS) of three spectrometers for the ExoMars 2016 Trace Gas Orbiter. Space Sci. Rev., 214, pp.1-62.

McCleese, D.J., Schofield, J.T., Taylor, F.W., Calcutt, S.B., Foote, M.C., Kass, D.M., Leovy, C.B., Paige, D.A., Read, P.L. and Zurek, R.W., 2007. Mars Climate Sounder: An investigation of thermal and water vapor structure, dust and condensate distributions in the atmosphere, and energy balance of the polar regions. J. Geophys. Res.: Planets, 112(E5).

Millour, E., Forget, F., González-Galindo, F., Spiga, A., et al., 2009. The Mars Climate Database (version 4.3). SAE Technical Paper 2009-01-2395. http://dx.doi.org/10.4271/2009-01-2395.

Montmessin, F., Forget, F., Rannou, P., Cabane, M., and Haberle, R. M., 2004. Origin and role of water ice clouds in the Martian water cycle as inferred from a general circulation model. J. Geophys. Res.: Planets, 109(10), 1–26. https://doi.org/10.1029/2004JE002284

Montmessin, F., and 27 co-authors, 2017. SPICAM on Mars Express: A 10 year in-depth survey of the Martian atmosphere. Icarus, 297, pp.195-216.

Murchie, S., Arvidson, R., Bedini, P., Beisser, K., Bibring, J.P., Bishop, J., Boldt, J., Cavender, P., Choo, T., Clancy, R.T. and Darlington, E.H., 2007. Compact reconnaissance imaging spectrometer for Mars (CRISM) on Mars reconnaissance orbiter (MRO). J. Geophys. Res.: Planets, 112(E5).

Navarro, T., Madeleine, J.B., Forget, F., Spiga, A., Millour, E., Montmessin, F. and Määttänen, A., 2014. Global climate modeling of the Martian water cycle with improved microphysics and radiatively active water ice clouds. J. Geophys. Res.: Planets, 119(7), pp.1479-1495.

Pankine, A.A., 2015. The nature of the systematic radiometric error in the MGS TES spectra. Planet. Space Sci., 109, pp.64-75.

Pankine, A.A., 2016. Radiometric error and re-calibration of the MGS TES spectra. Planet. Space Sci., 134, pp.112-121.

Pankine, A., 2020. Mars Global Surveyor Thermal Emission Spectrometer –recalibrated, NASA Planetary Data System,https://doi.org/10.17189/1518963.[WWW Document] URL (https://pds-atmospheres.nmsu.edu/data_and_services/atmospheres_data/MARS/pankine_data.html) (accessed 2.16.2022)

Pankine, A., 2022a. Mars Global Surveyor Thermal Emission Spectrometer Atmospheric Recalibration Bundle, NASA Planetary Data System, https://doi.org/10.17189/xhqz-zw13. [WWW Document] URL (https://pds.nasa.gov/ds-view/pds/viewBundle.jsp?identifier=urn%3Anasa%3Apds%3Amgs_tes_recalib_atmos&version=1.0) (accessed 3.13.2023)

Pankine, A.A., 2022b. Martian atmospheric water vapor abundances in MY26-30 from Mars Express PFS/LW observations. Icarus, 379, p.114975.

Pankine, A., (July, 2023). "Water vapor abundances, dust opacities and surface temperatures in the second half of Mars Years 24, 25, 28, 29, 34 in the Southern Polar Region of Mars." [Dataset], Mendeley Data, V1, doi: 10.17632/mk4bs7v9x9.1

Pankine, A. A., and Tamppari, L. K., 2019. MGS TES observations of the water vapor in the Martian southern polar atmosphere during spring and summer. Icarus, 331(February), 26–48.https://doi.org/10.1016/j.icarus.2019.05.010

Pankine, A.A., Bandfield, J.L., McConnochie, T.H. and Rogers, A.D., 2023. Re-calibration of Mars Global Surveyor Thermal Emission Spectrometer spectra. 1. Methodology and re-derived data products: Aerosol opacities and surface emissivities. Planet. Space Sci., p.105673. https://doi.org/10.1016/j.pss.2023.105673

Piqueux, S., Kleinböhl, A., Hayne, P.O., Kass, D.M., Schofield, J.T. and McCleese, D.J., 2015. Variability of the Martian seasonal CO2 cap extent over eight Mars Years. Icarus, 251, pp.164-180.

Richardson, M.I. and Wilson, R.J., 2002. Investigation of the nature and stability of the Martian seasonal water cycle with a general circulation model. J. Geophys. Res.: Planets, 107(E5), pp.7-1.

Savijärvi, H., McConnochie, T.H., Harri, A.M. and Paton, M., 2019. Annual and diurnal water vapor cycles at Curiosity from observations and column modeling. Icarus, 319, pp.485-490.

Savijärvi, H., Martinez, G., Harri, A.M. and Paton, M., 2020. Curiosity observations and column model integrations for a Martian global dust event. Icarus, 337, p.113515.

Seelos, F.P., Seelos, K.D., Murchie, S.L., Novak, M.A.M., Hash, C.D., Morgan, M.F., Arvidson, R.E., Aiello, J., Bibring, J.P., Bishop, J.L. and Boldt, J.D., 2023. The CRISM investigation in Mars orbit: Overview, history, and delivered data products. Icarus, p.115612.

Smith, M.D., 2004. Interannual variability in TES atmospheric observations of Mars during 1999–2003. Icarus, 167(1), pp.148-165.

Smith, M.D., 2008. Spacecraft observations of the Martian atmosphere. Annu. Rev. Earth Planet. Sci., 36, pp.191-219.

Smith, M.D., 2009. THEMIS observations of Mars aerosol optical depth from 2002–2008. Icarus, 202(2), pp.444-452.

Smith, M.D., Daerden, F., Neary, L., and Khayat, A., 2018. The climatology of carbon monoxide and water vapor on Mars as observed by CRISM and modeled by the GEM-Mars general circulation model. Icarus, 301, 117–131. https://doi.org/10.1016/j.icarus.2017.09.027

Steele, L.J., Lewis, S.R., Patel, M.R., Montmessin, F., Forget, F., and Smith, M.D., 2014. The seasonal cycle of water vapour on Mars from assimilation of thermal emission spectrometer data. Icarus, 237, 97–115. https://doi.org/10.1016/j.icarus.2014.04.017

Trokhimovskiy, A., Fedorova, A., Korablev, O., Montmessin, F., Bertaux, J.L., Rodin, A. and Smith, M.D., 2015. Mars' water vapor mapping by the SPICAM IR spectrometer: Five Martian years of observations. Icarus, 251, pp.50-64.

Tschimmel, M., Ignatiev, N. I., Titov, D. V., Lellouch, E., Fouchet, T., Giuranna, M., and Formisano, V. (2008). Investigation of water vapor on Mars with PFS/SW of Mars Express. Icarus, 195(2), 557–575. https://doi.org/10.1016/j.icarus.2008.01.018

Vandaele, A.C., Neefs, E., Drummond, R., Thomas, I.R., Daerden, F., Lopez-Moreno, J.J., Rodriguez, J., Patel, M.R., Bellucci, G., Allen, M. and Altieri, F., 2015. Science objectives and performances of NOMAD, a spectrometer suite for the ExoMars TGO mission. Planet. Space Sci., 119, pp.233-249.

Vandaele, A.C., and co-authors, 2019. Martian dust storm impact on atmospheric $H_2O$ and D/H observed by ExoMars Trace Gas Orbiter. Nature, 568(7753), 521–525. https://doi.org/10.1038/s41586-019-1097-3

Wolff, M.J. and Clancy, R.T., 2003. Constraints on the size of Martian aerosols from Thermal Emission Spectrometer observations. J. Geophys. Res.: Planets, 108(E9).

Wolkenberg, P., Giuranna, M., Smith, M.D., Grassi, D. and Amoroso, M., 2020. Similarities and differences of global dust storms in MY 25, 28, and 34. J. Geophys. Res.: Planets, 125(3), p.e2019JE006104.